JOURNAL OF GEOPHYSICAL RESEARCH, VOL. 107, NO. D20, 8292, doi:10.1029/2001JD001025, 2002

In situ observations of gravity waves and comparisons with numerical simulations during the SOLVE/THESEO 2000 campaign

A. Hertzog,[1] F. Vial,[1] A. Dörnbrack,[2] S. D. Eckermann,[3] B. M. Knudsen,[4]
and J.-P. Pommereau[5]

Received 5 July 2001; revised 28 December 2001; accepted 20 March 2002; published 18 October 2002.

[1] This article presents observational and numerical results on gravity waves in the Arctic polar vortex during the SAGE III—Ozone Loss and Validation Experiment and Third European Stratospheric Experiment on Ozone 2000 (SOLVE/THESEO) campaign. Long-duration balloons that were launched from Kiruna, Sweden, on 18 February 2000 provided in situ meteorological measurements for several weeks in the lower stratosphere. A strong gravity wave event was observed above southern Scandinavia on 2 March 2000. The main characteristics (amplitude of disturbances, frequency, and wavelengths) are reported, and it is shown that the wave induced mesoscale temperature fluctuations were large (18 K peak to peak). Furthermore, it is found that the gravity wave was most likely generated by flow across the Norwegian mountains. The observations are compared with results of numerical simulations. In particular, the mesoscale and ray-tracing simulations reproduced some features of the observed wave packet. However, the fluctuations induced by the wave were significantly underestimated in the general circulation model of the European Center for Medium-Range Weather Forecasting. Finally, the overall gravity wave activity during the flight is analyzed and is found to be relatively small. *INDEX TERMS:* 3329 Meteorology and Atmospheric Dynamics: Mesoscale meteorology; 3334 Meteorology and Atmospheric Dynamics: Middle atmosphere dynamics (0341, 0342); 3384 Meteorology and Atmospheric Dynamics: Waves and tides; *KEYWORDS:* polar stratosphere, gravity waves, mesoscale processes, mesoscale modeling, long-duration balloons

Citation: Hertzog, A., F. Vial, A. Dörnbrack, S. D. Eckermann, B. M. Knudsen, and J.-P. Pommereau, In situ observations of gravity waves and comparisons with numerical simulations during the SOLVE/THESEO 2000 campaign, *J. Geophys. Res.*, *107*(D20), 8292, doi:10.1029/2001JD001025, 2002.

1. Introduction

[2] Ozone depletion inside the winter stratospheric vortex is a complex process that results from a conjunction of dynamical, chemical and radiative causes [*Solomon*, 1999]. One key step in this process is the formation of polar stratospheric clouds (PSCs), on which bromine and chlorine inert species are converted into active species [*Peter*, 1997]. These active species are involved in the catalytic ozone-depletion cycles that are triggered when air masses encounter sunlit conditions. However, PSCs can form only when the air temperature falls below a certain threshold that depends on the exact PSC composition. Such low-temperature conditions are commonly present within the Antarctic vortex, where the ozone-depletion process is very effective. On the other hand, the Arctic vortex is disturbed and displaced by planetary waves generated by the northern hemisphere land/ocean contrasts and major orographic systems. Consequently, the Arctic vortex is warmer and the conditions for the formation of PSC are less frequent than for the southern-hemisphere vortex [e.g., *Pawson et al.*, 1995].

[3] Thus, in the Arctic vortex, mesoscale processes that induce temperature fluctuations may enhance PSCs and modify their composition. Among those processes, gravity waves generated by flow over mountains are believed to be of some importance [e.g., *Gary*, 1989; *Carslaw et al.*, 1998a; *Dörnbrack et al.*, 2001; *Dörnbrack and Leutbecher*, 2001]. However, little is known about the global-scale activity of gravity waves in the Arctic vortex.

[4] In that context, one of the goals of the SOLVE/THESEO 2000 campaign that took place in Kiruna, Sweden during the 1999/2000 winter was to improve our knowledge of mesoscale processes in the polar vortex. In particular, long-duration balloons that are able to drift for several weeks in the lower stratosphere were launched during this campaign. The balloons (infrared Montgolfière or MIR) were carrying gondolas designed to measure the concentration of chemical species involved in ozone depletion [*Pommereau et al.*, 2002; *Knudsen et al.*, 2001]. However, meteorological in situ measurements were also made,

---

[1] Laboratoire de Météorologie Dynamique, Palaiseau, France.

[2] Deutschen Zentrum für Luft- und Raumfahrt, Oberpfaffenhofen, Germany.

[3] Naval Research Laboratory, Washington, D. C., USA.

[4] Danish Meteorological Institute, Copenhagen, Denmark.

[5] Service d'Aéronomie, Verrières-le-Buisson, France.

0148-0227/02/2001JD001025$09.00

allowing a global view of gravity wave activity inside the Arctic polar vortex.

[5] Some efforts have been made recently to quantify the impact of gravity waves on PSC formation [*Murphy and Gary*, 1995; *Wirth and Renger*, 1996; *Carslaw et al.*, 1998b; *Bacmeister et al.*, 1999; *Carslaw et al.*, 1999; *Rivière et al.*, 2000]. These results have been obtained with the help of parameterizations or mesoscale models that are able to simulate small-scale mountain waves. The balloonborne measurements recorded during the SOLVE/THESEO 2000 campaign offer the possibility to compare gravity wave observations with corresponding numerical simulations, and therefore help to validate the models.

[6] In this study, we report on dynamical in situ measurements made in February and March 2000 in the Arctic stratosphere during one of the MIR flights. We first focus on 2 March 2000, when strong gravity wave disturbances were observed by the MIR south of the Scandinavian Peninsula. In particular, the observed temperature and cooling rate fluctuations, which are of primary importance in determining the PSC composition, are reported and compared with the corresponding numerical simulations from mesoscale, general circulation and ray-tracing models. Then we give an over-view of gravity wave activity in the Arctic polar vortex during this MIR flight. The article is organized as follows. Section 2 is dedicated to the presentation of the balloon flights and measurements. The main characteristics of the models used in this study are also briefly reported. In section 3, we present the March 2 2000 gravity wave case study, as it appears in the observations and in the simulations. Section 4 is devoted to the analysis of the global-scale gravity wave activity measured during the flight. Finally, concluding remarks are given in section 5.

2. Data Sets

2.1. Balloons

[7] Two infrared Montgolfière (MIR) (i.e., open balloons that are partly aluminized) were launched in February 2000 from Kiruna (67.9°N, 21.1°E), Sweden. A complete description of the flights is given by *Pommereau et al.* [2002]. Only short descriptions of the gondolas and of the different meteorological sensors they carried are presented in this paper. The MIRs were launched on the same day (18 February 2000), when the vortex was passing over Kiruna. Balloons are allowed to fly only north of 55°N, due to security considerations. Unfortunately, the first MIR flew southward of 55°N after only two days, limiting therefore the scientific interest of that flight.

[8] However, the second MIR flew for 18 days in the polar vortex. Its trajectory is shown in Figure 1. The MIR made four revolutions in the vortex and flew both above mountain ranges (e.g., Scandinavia, Urals, Greenland, Spitzbergen) and above flat areas (e.g., ocean, ice-pack, western Siberia).

[9] The altitude of the MIR is controlled by the temperature of the air inside the balloon, which is heated by the balloon envelope. The envelope absorbs the solar flux during the day and the telluric infrared flux at night. Consequently, the MIR altitude is higher during the day than at night and the MIR exhibits vertical excursions at sunrise and sunset.

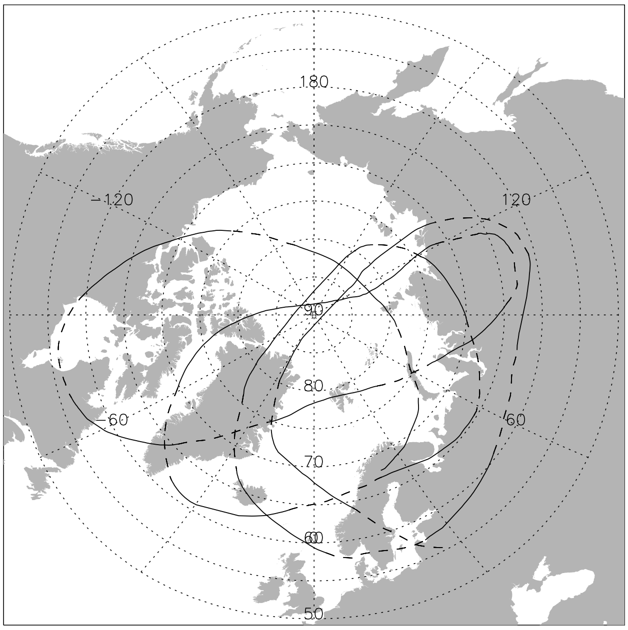

Figure 1. Trajectory of the second MIR. The MIR was launched from Kiruna, Sweden on 18 February 2000 and was destroyed over Belarus on 8 March 2000 after 18 days of flight. Daytime sections of the flight are dashed.

[10] The MIR carried two gondolas: Salsa, a gondola hosting several instruments measuring stratospheric minor species (a SAOZ-UV visible spectrometer, a tunable-diode laser to measure CH_4 and a Lyman α hygrometer) and Samba, the French Space Agency (CNES) gondola, that was responsible for meteorological measurements and for the flight security. In this paper, we will focus on analysis of the purely dynamical measurements. *Pommereau et al.* [2002] and *Vial et al.* [2001] reported on the accuracy of the various meteorological sensors: Briefly, the wind velocity is deduced from successive GPS 3-D positions and the accuracy is better than 0.3 m s^{-1}; successive pressure measurements are obtained with a 0.1 hPa precision (the pressure accuracy is known to about 1 hPa), and temperature measurements are made during night and sunset with an accuracy of 0.5 K (during daylight hours, the temperature sensors are perturbed by solar radiation and by heat emitted from the gondola and will not be used in this study). Measurements were obtained every 10 min along the flight track. Some GPS points were not correctly recorded during vertical-excursion phases, resulting in some missing wind-velocity measurements at sunrise and sunset.

[11] The ability of long-duration balloons to track stratospheric perturbations due to gravity waves was demonstrated by *Massman* [1978, 1981], *Vial et al.* [2001], and *Hertzog and Vial* [2001]. These authors showed that the Lagrangian data they provide could be analyzed to provide direct measurements of the intrinsic frequencies of gravity waves, as well as other wave quantities. Intrinsic frequencies cannot be measured directly from ground-based or airborne instruments [e.g., *Fritts and VanZandt*, 1987; *Vincent and Eckermann*, 1990; *Bacmeister et al.*, 1996], and so this important wave parameter can only be inferred using more indirect data analysis methods [e.g., *Hirota and Niki*, 1985; *Cot and Barat*,

1986; *Eckermann*, 1996; *Dean-Day et al.*, 1998] which can be subject to various interpretative uncertainties [e.g., *Eckermann and Hocking*, 1989; *Hines*, 1989]. Thus we have no direct measurements of gravity wave intrinsic frequencies, which are essential to assess, for instance, wave induced cooling rates [*Bacmeister et al.*, 1999].

2.2. Models

2.2.1. MM5

[12] Simulations are performed using the MM5 three-dimensional nonhydrostatic mesoscale model [*Dudhia*, 1993; *Grell et al.*, 1994]. The outer model domain is centered around 10°E, 60°N with an extension of 2208 km × 2208 km. In this domain, the horizontal grid size is 24 km. A local grid refinement scheme with a horizontal grid size of 8 km is applied south of the Scandinavian peninsula to resolve most of the horizontal wave number spectrum of vertically propagating gravity waves excited by mountains. The model extends up to 30 km, where radiative boundary conditions avoid spurious vertical reflection of waves. Simulated fields are stored every two hours.

2.2.2. ECMWF

[13] We will also compare our observations with general circulation simulations performed with the European Center for Medium-Range Weather Forecasting (ECMWF) model. The version used in this study is the T319 spherical-harmonic model. The simulated fields are extracted on a 0.4°latitude-longitude grid. The model has 60 levels in the vertical, up to 0.1 hPa and it assimilates the Advanced Microwave Sounding Unit data. To that purpose, a four-dimensional variational data assimilation scheme is used [*Rabier et al.*, 2000]. The analyses are available every 6 hours. To deal with the gravity wave drag forced by sub gridscale mountains the scheme by *Lott and Miller* [1997] is used. The model mountains are based on the GTOPO30 data at 30″ × 30″ resolution, but scales below about 5 km do not contribute.

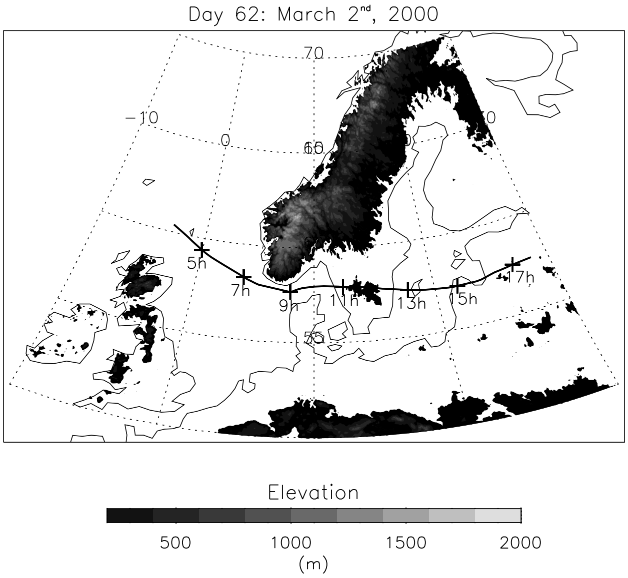

Figure 2. Trajectory of the infrared Montgolfière (bold curve) south of the Scandinavian Peninsula on 2 March 2000 (day 62 in 2000). Labels show universal times along the trajectory.

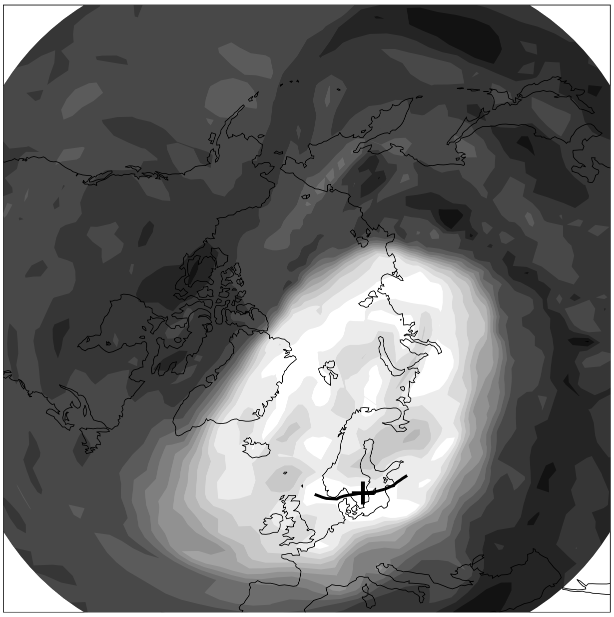

Figure 3. Potential vorticity (PV) on the 675 K isentropic surface on 2 March 2000 at 1200 UT from the ECMWF analysis. Darker areas correspond to low PV value (surf zone), while lighter areas correspond to high-PV values (polar vortex). The black cross, south of Sweden, indicates the position of the balloon at 1200 UT, and the balloon trajectory between 6000 and 1800 UT is also shown (bold curve).

2.2.3. Mountain Wave Forecast Model (MWFM)

[14] The model used here (MWFM 2.0) is a ray-based extension of the initial model developed by *Bacmeister et al.* [1994], which models mountain waves based on quasi-two dimensional fits to dominant ridge-like structures in Earth's topography. MWFM 2.0 incorporates a number of changes from the MWFM 1.0 model. Most importantly, it replaces the two-dimensional irrotational hydrostatic gravity wave model used in MWFM 1.0 with ray-tracing equations governed by a rotating nonhydrostatic dispersion relation. Wave amplitudes are governed by conservation of vertical flux of wave action density, and wave breaking thresholds due to dynamical and convective instabilities are parameterized. Peak temperature and horizontal velocity amplitudes are calculated from the wave action densities using standard polarization relations. The formulation is similar to that from *Marks and Eckermann* [1995]. Temporal and horizontal variations of the background atmosphere are ignored, so that ground-based wave phase speeds remain stationary. Three dimensionality in mountain wave patterns is also accommodated by launching waves at different azimuths, with maximum amplitudes perpendicular to the quasi-two-dimensional ridge axis and amplitude scaled from there, according to the three-dimensionality of the analyzed ridge feature. Thus MWFM 2.0 can parameterize important mountain wave effects that the old model could not, such as vertical reflection [e.g., *Schoeberl*, 1985], three-dimensional "ship wave" patterns [*Broutman et al.*, 2001] and down-stream dispersion due to nonhydrostatic or near-inertial

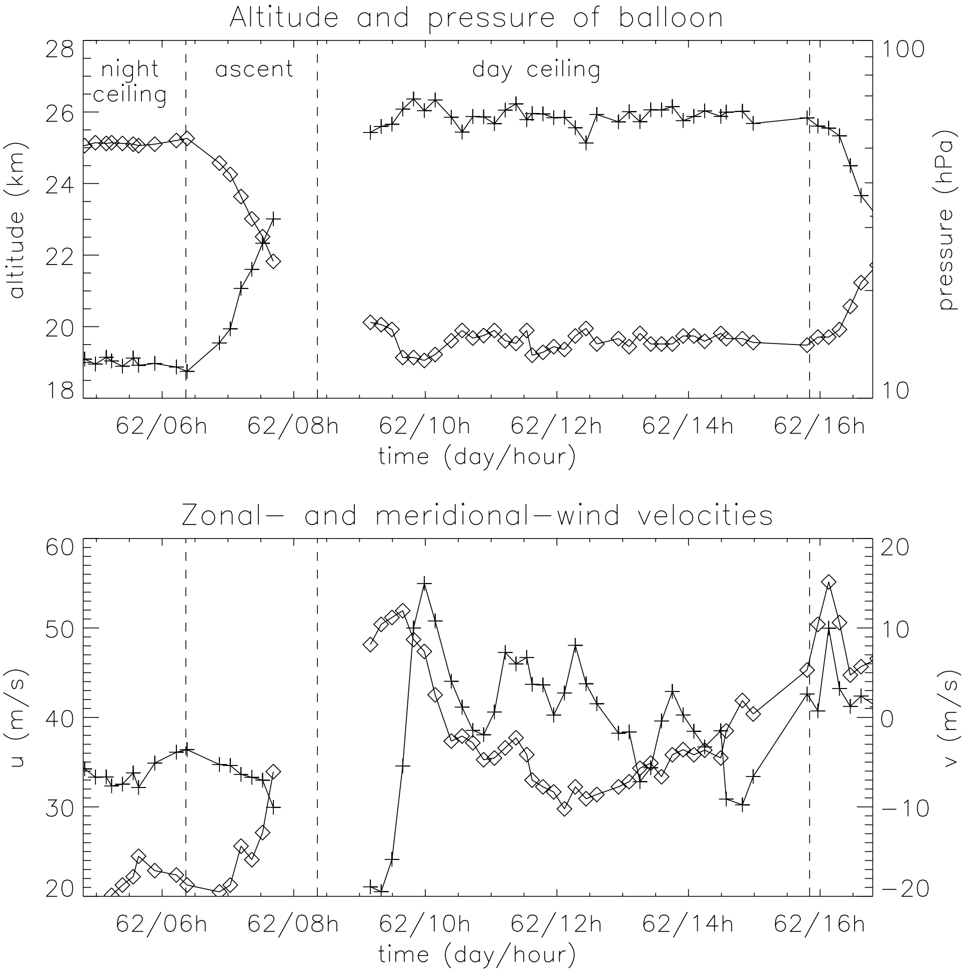

Figure 4. Upper panel: MIR altitude (cross, left scale) and measured atmospheric pressure (diamond, right scale) on 2 March 2000 (day 62 in 2000). Bottom panel: zonal (cross, left scale) and meridional (diamond, right scale) wind velocities. Each symbol (cross or diamond) corresponds to a measurement. Note that some GPS positions were lost during the balloon ascent at sunrise and at the beginning of the day ceiling.

effects. Both the 1.0 and 2.0 models (as well as MM5) were used in forecast mode throughout SOLVE/THESEO 2000.

[15] MWFM is a numerical mountain wave parameterization, unlike ECMWF and MM5 that model the entire atmospheric flow using the primitive equations, including any explicitly-resolved mountain waves. Additionally, MWFM focuses mostly on topographic features that are unresolved by most global models (i.e., sub gridscale), and thus typically simulates small-to-medium scale gravity waves with horizontal wavelengths in the 10–200 km range.

3. Case Study

3.1. Observations

[16] The event studied in this section occurred on 2 March 2000. At that time, the MIR was flying south of the Norwegian coast (see Figure 2) along the inner side of the main potential vorticity gradient (Figure 3). Note that it did not pass over the Norwegian mountains but flew until 1100 UT over the sea.

[17] Figure 4 shows the MIR altitude, pressure and velocities on this day. At approximately 0600 UT, the MIR began to ascend, as it encountered sunrise. After 0730 UT, some GPS positions were lost. The ascent finished by 0900 UT, when the GPS signal was recovered. Thereafter, the MIR flew at a roughly constant altitude of 26 km ± 500 m until ~1600 UT, when it encountered sunset and started its descent phase.

[18] Figure 4 shows that the balloon flew through a very large zonal wind disturbance at the beginning of the daytime ceiling (i.e., between 0900 UT and 1130 UT). The amplitude of the zonal velocity fluctuations is 17 ± 0.3 m s^{-1} (i.e., peak-to-peak fluctuations of 34 m s^{-1}). On the other hand, the meridional wind velocities exhibit peak-to-peak fluctuations of 14 m s^{-1}. Given the typical timescale of the fluctuations, we interpret this feature as a gravity wave intercepted by the balloon. Temperature measurements are unfortunately of poor quality since this event took place during the day. Therefore, in the following, we will only use the wind-velocity data to extract the wave characteristics.

[19] The wave packet intrinsic angular frequency (ω_0) is first evaluated at the beginning of the day ceiling (i.e., between 0900 and 1030 UT). Since the balloon does not exhibit large vertical excursions during that time interval

Table 1. Observed and Simulated Wave Packet Characteristics

	Intrinsic Period, min	Wavelengths		Direction of Propagation[a]	u', m s^{-1}	T', K	Maximum Cooling Rate, K h^{-1}
		Horizontal, km	Vertical, km				
Observations	80 ± 7	202[b] ± 21	10.5[c] ± 1.5	173° ± 1°	17 ± 0.3	9.1[d] ± 1.5	−43[d] ± 11
MM5	105	200	8	169°	17	11	−38
ECMWF	160	350	9	180°	3	1.5	−3.5
MWFM	90	200	10	165°	19	8	−33

[a] Angles are counted positively anticlockwise, and 0° corresponds to eastward propagation relative to the ground.
[b] Obtained by assuming that the wave is stationary relative to the ground.
[c] As in note[b], and applying the dispersion relationship for gravity waves.
[d] Obtained by applying the polarization relationships for gravity waves.

and is moreover advected by the mean wind, the period of the observed zonal wind fluctuations measured on board the balloon is the intrinsic period of the wave packet (i.e., the period relative to the mean flow). We obtain: $2\pi/\omega_0 \sim 75 \pm 5$ min. Another estimate of the wave intrinsic period can be obtained by the analysis of the horizontal velocity hodograph: The ratio between the ellipse long and short axes is equal to ω_0/f, where f is the inertial period [*Andrews et al.*, 1987]. In our case, this analysis (not shown) yields $2\pi/\omega_0 \sim 85 \pm 1$ min. We will therefore assume in the following that the intrinsic period of the wave packet is 80 ± 7 min.

[20] The inertial period ($2\pi/f$) at the balloon latitude (~58°) is ~14 h, while the Brunt-Väisälä frequency (N) estimated in the mesoscale MM5 simulations is $2.5\ 10^{-2}$ ±

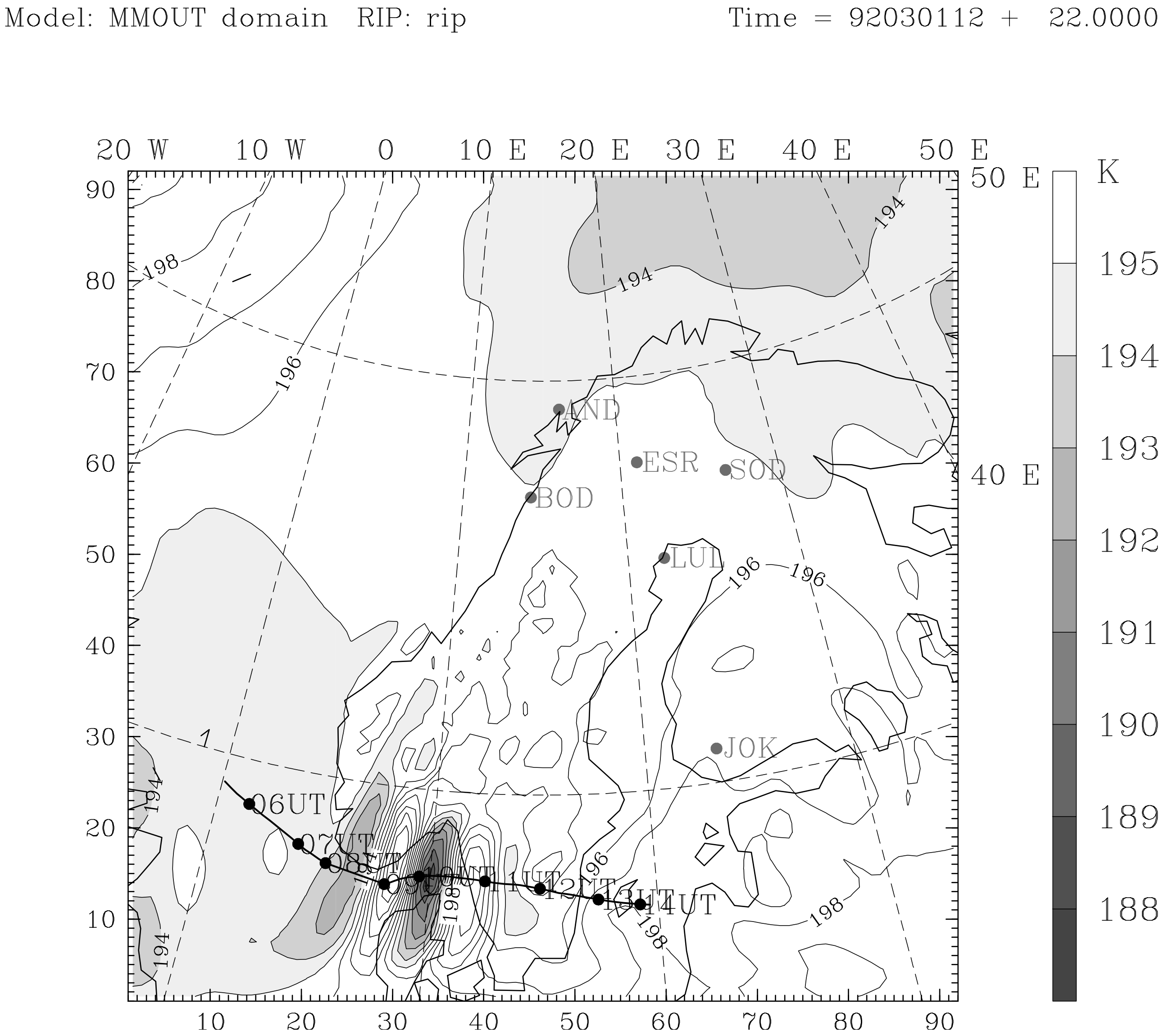

Figure 5. Temperature field simulated by the MM5 model at 30 hPa, on 2 March 2000, 1000 UT. The balloon trajectory is also shown. Note the presence of a gravity wave packet located over southern Norway.

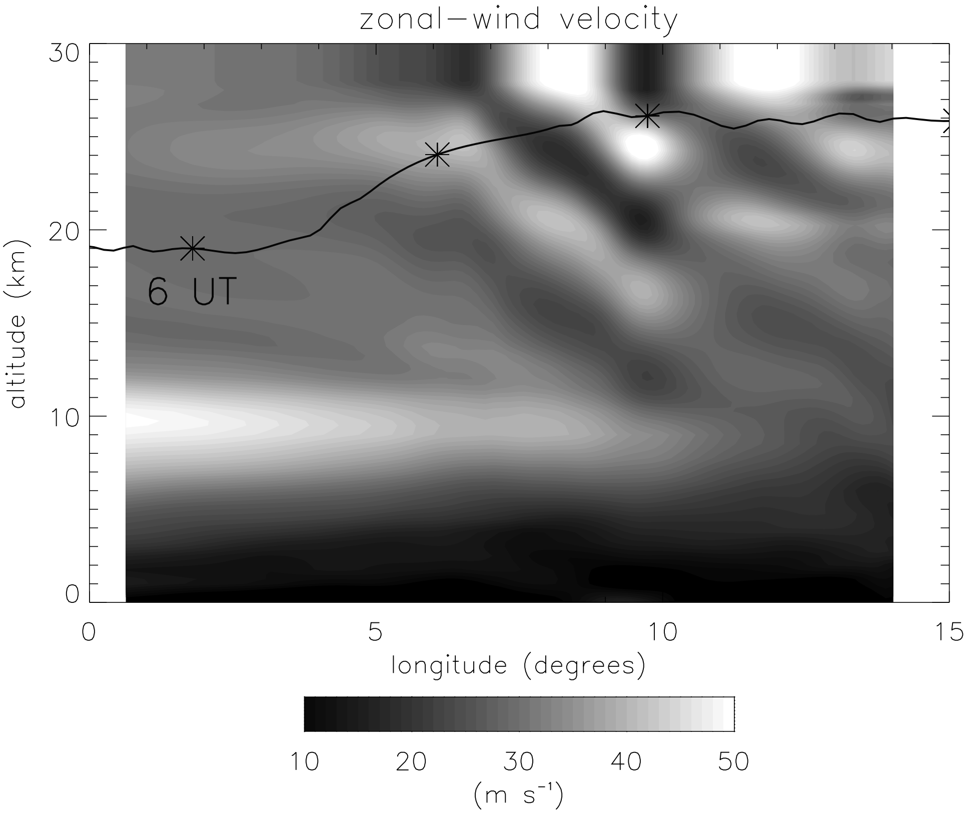

Figure 6. Cross section of the zonal wind velocity on 2 March 2000, 1000 UT, in the MM5 model. The cross section coincides with the balloon trajectory south of Norway. The balloon altitude as a function of time is shown by the solid black line. Stars are plotted every 2 h.

$0.3\ 10^{-2}$ rad s^{-1} in the lower stratosphere (corresponding to a period 4 min). Therefore we can apply the so-called midfrequency approximation.

$$|f| \ll |\omega_0| \ll N. \tag{1}$$

[21] Since the amplitude of the zonal velocity fluctuations is much larger than that of the meridional velocity fluctuations, the wave vector is almost zonally oriented. Indeed, the long axis of the hodograph, which is parallel to the wave vector, is oriented 7° off the zonal direction, either north of due west or south of due east. The wind-velocity fluctuations (u') are thus linked to the amplitude of the temperature disturbance (T') by the polarization relationship [*Andrews et al.*, 1987]:

$$T' = T_0 \frac{N}{g} u', \tag{2}$$

where T_0 is the background temperature, which was estimated from the measurements made during sunset (i.e., at the same altitude as the daytime ceiling but in the absence of solar radiation) to be 210 ± 4.5 K. Hence we obtain: T' = 9.1 ± 1.5 K (i.e., peak-to-peak fluctuations of ~18 K). Finally, the maximum (reversible) cooling rate induced by the wave (T'_t) can be computed as:

$$T'_t = -\omega_0 T' = -43 \pm 11\,\mathrm{K\,h^{-1}}. \tag{3}$$

[22] To get more insights into the characteristics of the wave packet, we will now assume that it was generated over the Norwegian mountains by a quasi-stationary flow. This assumption will be discussed later on. In this context, the wave packet is stationary relative to the ground, so that its intrinsic angular frequency is given by [*Andrews et al.*, 1987]:

$$\omega_0 = -\vec{k}_h . \vec{u}, \tag{4}$$

where $\vec{k}_h = (k, l)$ is the horizontal wave vector, and $\vec{u} = (u, v)$ the horizontal wind vector. In our case, this equation reduces to:

$$\omega_0 = -ku, \tag{5}$$

where $u \sim 42$ m s^{-1}. This yields a horizontal wavelength ($2\pi/|k|$) of 202 ± 21 km. Note that k is negative here, in order for the wave to be stationary relative to the ground, and consequently the wave vector is aligned 7° north of due west. Finally, the vertical wave number (m) is computed using the simplified midfrequency dispersion relationship for gravity waves:

$$m = \frac{N}{\omega_0} k = -\frac{N}{u}, \tag{6}$$

where we have assumed that the wave packet propagates upward (m and ω_0 have opposite signs). It yields a vertical wavelength ($2\pi/|m|$) of 10.5 ± 1.5 km. This vertical wavelength is relatively large: Classical spectra show highest values of energy density at about $2\pi/m_* = 2-4$

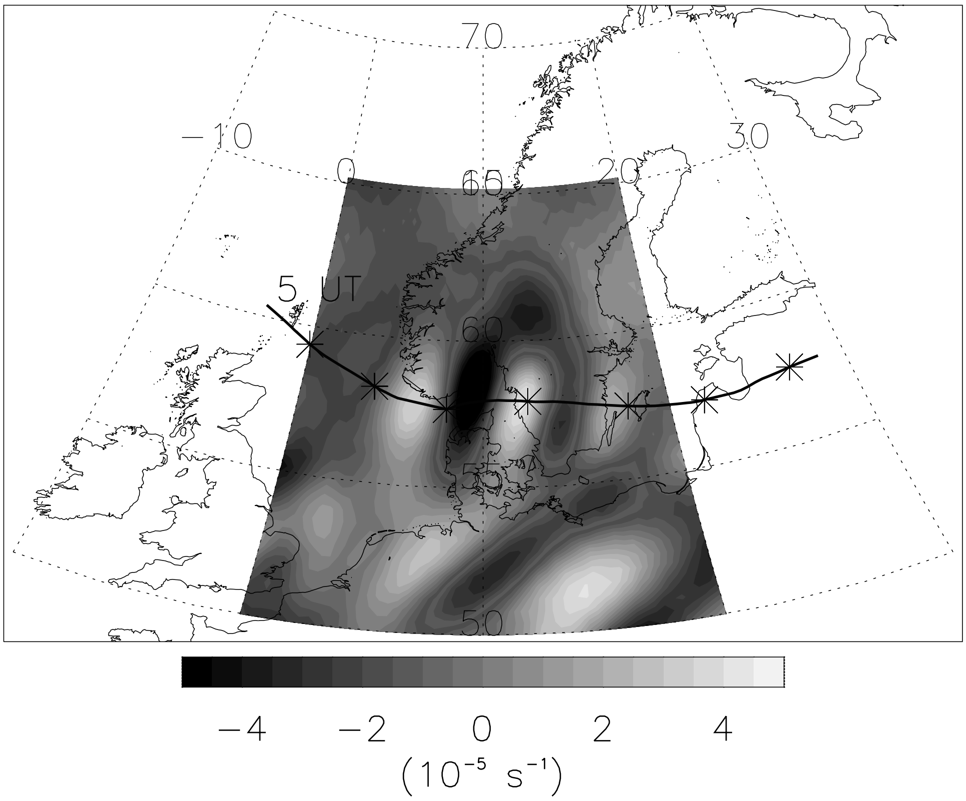

Figure 7. Divergence of the horizontal wind velocity simulated by the ECMWF T319 model at 20 hPa on 2 March 2000, 1200 UT. The trajectory of the balloon is shown in green and stars are plotted every 2 h. See color version of this figure at back of this issue.

km in the lower stratosphere [e.g., *Allen and Vincent*, 1995]. However, we have to stress that this long wavelength is needed to prevent static (and even dynamic) instabilities from developing, given the amplitude of the temperature fluctuations [see, e.g., *Eckermann and Preusse*, 1999]. For instance, the minimum value reached by temperature vertical gradients induced by the wave packet is $mT' \sim -5.5$ K km^{-1}, which does not exceed the dry adiabatic lapse rate (-10 K km^{-1}). On the other hand, the wave packet vertical wavelength is not so large that the factor $1/4H^2$ needs to be included in (6), where H is the density scale height of the atmosphere. Indeed, we can consider that $|m| \gg 1/2H$, with $H \sim 6$ km in the lower stratosphere.

[23] All the characteristics of the observed wave packet are reported in Table 1. In the following section, we analyze the wave packet as it is simulated in different dynamical models and compare the simulated characteristics with the observed ones.

3.2. Simulations

3.2.1. MM5

[24] The simulated temperature field at 30 hPa produced by the MM5 model, on 2 March 2000, 1000 UT is shown on Figure 5. The model obviously succeeded in producing a gravity wave packet at the geographical location where and time when the balloon was flying south of Norway. (Note, however, that the balloon was flying 2 km higher.) Two and a half wavelengths are clearly visible. In the model, the disturbances of the background fields induced by the wave packet maximize at 1000 UT (Figure 5). In the balloon data, the maximum amplitude was also observed at that time. This correspondence supports an interpretation of the simulated and the observed gravity wave as being the same event and that it is therefore meaningful to compare the characteristics of both waves.

[25] The zonal wind field simulated by the MM5 model at 1000 UT, as a function of longitude and altitude and on a cross section that coincides with the balloon trajectory south of the Scandinavian peninsula, is shown in Figure 6.

[26] The wave packet appears in this figure as tilted isocontours, east of 5°E and above 10 km. The amplitude of the disturbances is increasing with altitude up to ~27 km. Indeed, a strong numerical damping is imposed in the uppermost layers of the model, in order to avoid reflection of waves at the top of the simulation. This damping prevents vertical propagationof the wave packet beyond 27 km. Note that the tilt of isocontours is consistent with a gravity wave propagating upward and westward relative to the wind, i.e., the vertical phase speed of the wave is negative, while its vertical group velocity is positive.

[27] The balloon trajectory encounters the simulated gravity wave packet at 0800 UT, i.e., at the time when GPS points were lost (see Figure 4). The center of the wave packet is reached at 1000 UT, as in the observations. The characteristics of the simulated wave packet are also reported in Table 1. The amplitude of the zonal velocity fluctuations, the horizontal wavelength and the propagation direction are well reproduced by the model. On the other

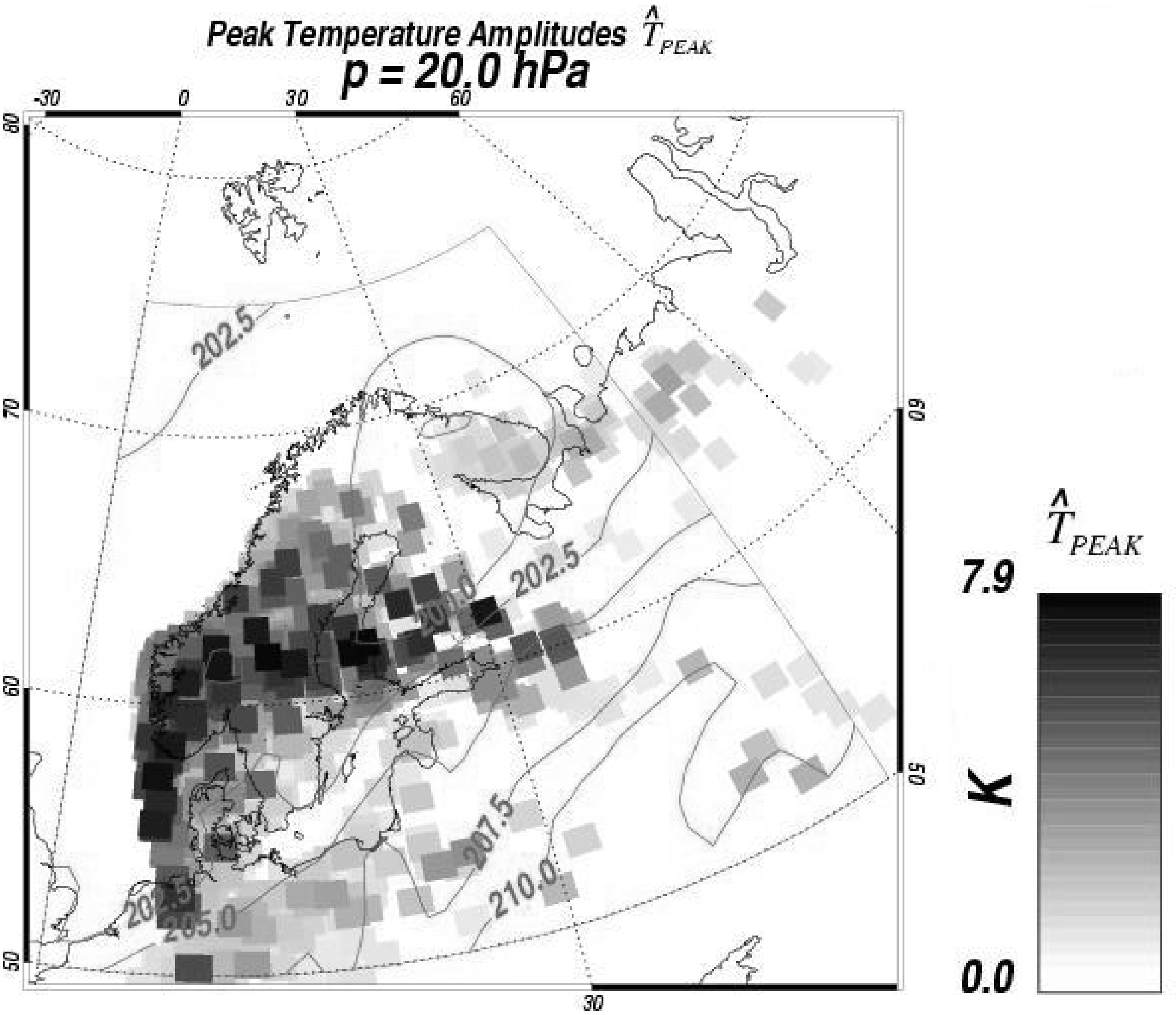

Figure 8. MWFM simulation of peak temperature amplitudes at 20 hPa on 2 March 2000, 0000 UT (colored squares). Each pixel represents the group location and amplitude of a ray. DAO analyzed background temperatures are represented as contours (labels in K). See color version of this figure at back of this issue.

hand, the period of the wave is 15 min longer in themodel, whereas the vertical wavelength is shorter and the amplitude of the temperature fluctuations are overestimated by ~2 K.

[28] In conclusion, the simulated location, time, and characteristics of the wave packet are in fair agreement with the observations. The discrepancies that are observed could be at least partly due to the limited resolution of the model, the friction that is applied and the presence of the top boundary close to the wavepacket [*Leutbecher and Volkert*, 2000].

3.2.2. ECMWF

[29] The divergence of the horizontal wind at 20 hPa simulated by the ECMWF T319 model on 2 March 2000, 1200 UT is shown on Figure 7. This field easily enables us to identify gravity wave packets in general circulation models [e.g., *O'Sullivan and Dunkerton*, 1995; *Moldovan et al.*, 2002]. In our case the gravity wave, through which the MIR flew south of Norway, is also captured by the ECMWF simulation. Furthermore, the phase structure and the geographical localization of the wave packet compare well with the MM5 simulations (see Figure 5).

[30] The wave packet characteristics in the ECMWF simulation are reported in Table 1. The vertical wavelength and the propagation direction agree fairly well with the observations. However, several differences between the simulation and the observations are obvious. In particular, the horizontal wavelengths and the period of the wave packet are overestimated by a factor of 2 in the ECMWF simulation.

[31] The main discrepancy is in the amplitudes of the disturbances, which are much lower in the ECMWF fields than observed in the MIR data. First, it should be noticed that the vertical resolution of the model is relatively coarse in the stratosphere (around 1 km at 25 km), so that gravity waves may be poorly simulated even though the horizontal and temporal resolutions are high enough. For the case considered however, the vertical wavelength of the wave packet is much larger than1 km so that the this effect is

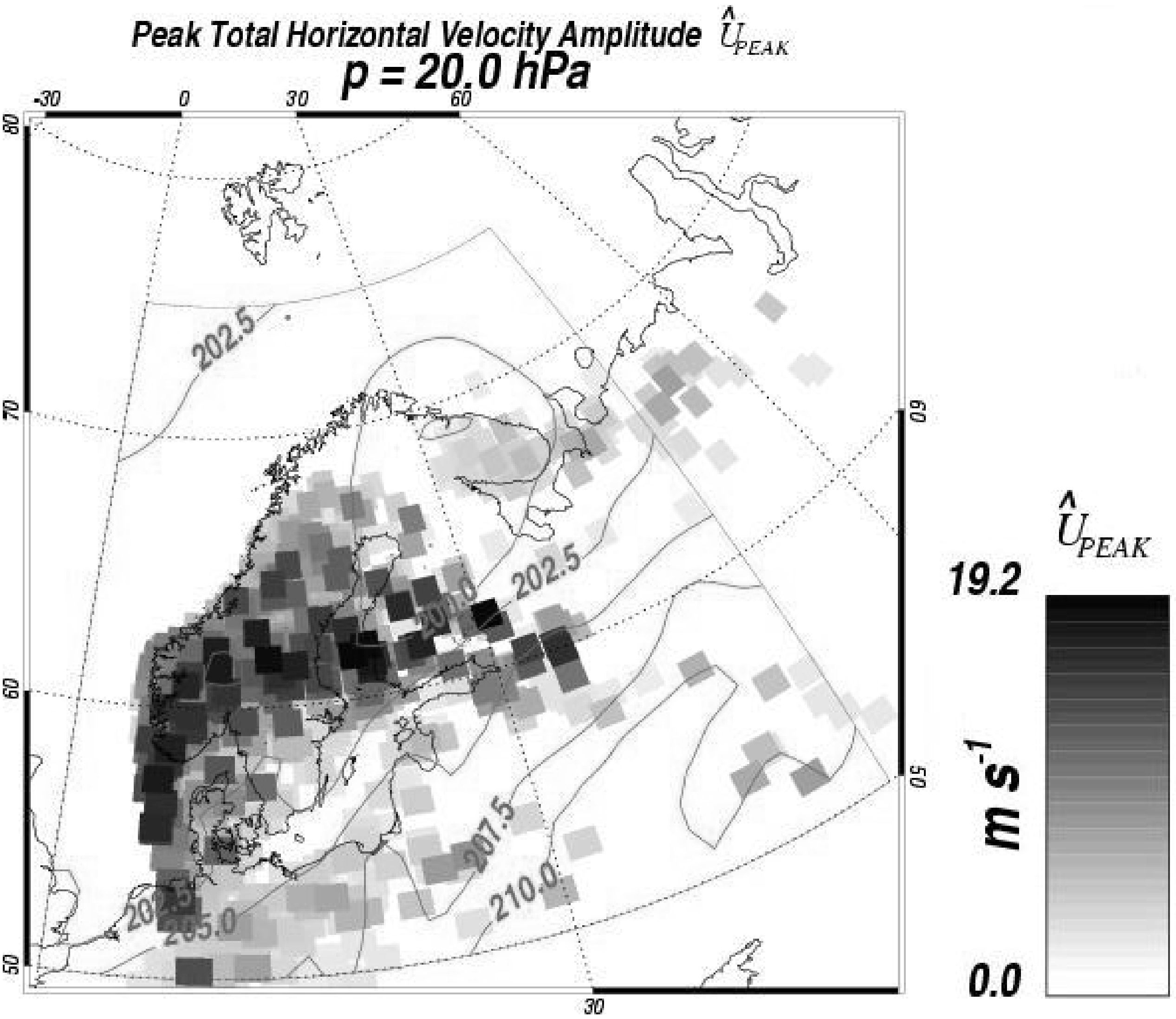

Figure 9. Same as Figure 8 but for the horizontal velocity. See color version of this figure at back of this issue.

expected to be small. The most likely explanation is that a filtering is applied in the model to exclude the disturbances that induce strong divergence. This is done in order to avoid spurious energy transfer toward the smallest simulated scales, which may cause the model to diverge. Consequently, disturbances induced by gravity waves may be severely damped.

3.2.3. MWFM

[32] Figures 8 and 9 show hindcasts of peak amplitudes of temperature ($\hat{T}_{\mathrm{PEAK}}$) and total horizontal velocity ($\hat{U}_{\mathrm{PEAK}}$), based on "late look" analysis winds and temperatures for 2 March 2000 at 0000 UT from NASA's Data Assimilation Office (DAO) [*Coy and Swinbank*, 1997]. Fifty-four rays were launched from each ridge feature: 3 individual horizontal wavelengths each launched at 18 equally spaced azimuths. Total horizontal wave numbers were calculated as

$$k_h = 1.5\ J/\Delta h, \tag{7}$$

where Δh is the width of the short axis of the ridge feature, and $J = 1, 2, 3$: These assignments are tunable but are close to peak responses found for simple analytical mountain profiles [e.g., *Broutman et al.*, 2001].

[33] We see from Figures 8 and 9 that MWFM predicts large-amplitude mountain waves at 20 hPa south of Scandinavia over open ocean on this day, as observed by the MIR. However, the maximum amplitude of the fluctuations in Figures 8 and 9 is located ~2° westward of the place where either the wave packet center is observed or the maximum temperature fluctuations are simulated by MM5 (Figure 5). The time difference between the MWFM fields (valid at 0000 UT) and the wave packet observation at 0930 UT can be responsible for part of the geographical discrepancy if the wave is not perfectly stationary. Furthermore,the westward tilt of the phase fronts with altitude (Figure 6) partly explains the differences between the MWFM and MM5 fields, since the former are plotted at 20 hPa whereas the latter are plotted at 30 hPa.

[34] Figure 10 shows scatterplots of the horizontal and vertical wavelengths and intrinsic period of rays as a function of their horizontal wave vector alignments, in the region 5–25°E and 54–58°N. Symbol sizes are propor-

tional to $\hat{T}^2_{\mathrm{PEAK}}$ for each ray. The largest amplitude mountain wave rays are aligned ~10–20° south of due east. The peak wavelengths and periods are similar to those observed, as summarized in Table 1.

3.3. Discussion

[35] In this section, we look more carefully on the mechanism that generated the wave packet observed by the balloon. To do this, we use the ECMWF T319 simulation. It has been assumed in section 3.1 that the gravity-packet was generated by the interaction between the Norwegian mountains and the flow close to the ground. First, it should be noted that the Norwegian mountains are a significant orographic system (the highest peak is located in the southern part of the system and has an altitude greater than 2000 m ASL). Furthermore, on 2 March 2000, 0000 UT, the low-level wind was blowing from the northwest on the western side of the mountains, i.e., perpendicular to the main ridge axis (not shown). At 700 hPa, the wind speed reached values of ~20 m s^{-1}, so that favorable conditions for the generation of mountain waves were present.

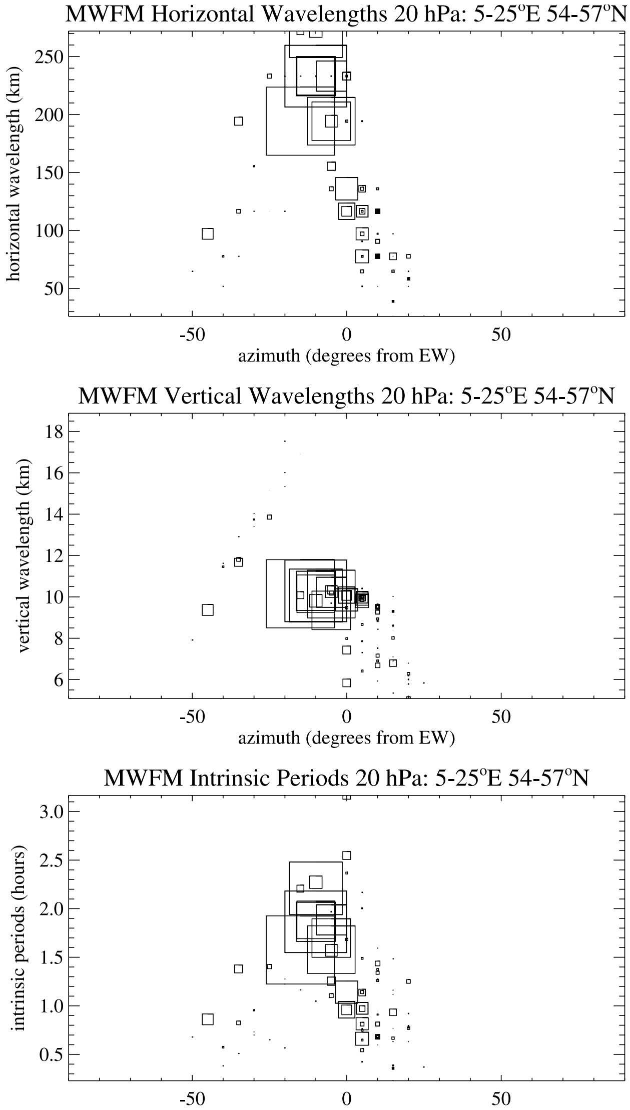
MWFM Horizontal Wavelengths 20 hPa: 5-25°E 54-57°N

MWFM Vertical Wavelengths 20 hPa: 5-25°E 54-57°N

MWFM Intrinsic Periods 20 hPa: 5-25°E 54-57°N

Figure 10. Scatterplots of horizontal wavelengths (upper panel), vertical wavelengths (middle panel), and intrinsic periods (lower panel) of rays simulated by the MWFM model above southern Scandinavia. The size of the symbols is proportional to the square of the temperature fluctuations associated with each ray.

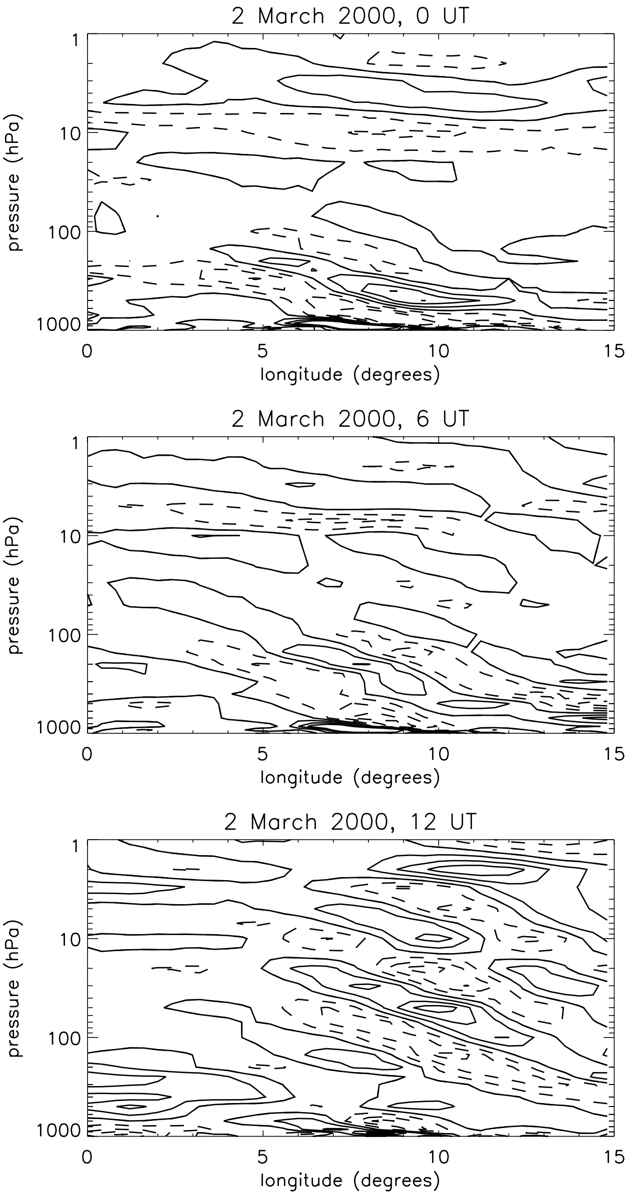
2 March 2000, 0 UT

2 March 2000, 6 UT

2 March 2000, 12 UT

Figure 11. Divergence of the horizontal wind velocity simulated by the ECMWF T319 model at 59°N, on 2 March 2000, 0000 UT (top), 0600 UT (middle), and 1200 UT (bottom). Contours are plotted every 2 × 10^{-5} s^{-1}, and contours associated with negative values are dashed.

[36] To be observed by the balloon, the wave packet had to propagate upward from the troposphere to the stratosphere. In order to follow this propagation, longitude-altitude cross sections at 59°N of the divergence of the ECMWF horizontal velocity on 2 March 2000 are shown in Figure 11. The wave packet propagates from the ground (between 5°E and 10°E, i.e., southern Norway) at 0000 UT to the stratosphere at 1200 UT, where it is observed by the MIR.

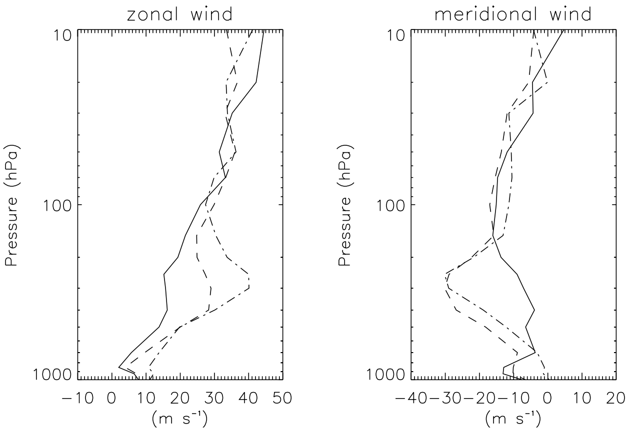

Figure 12. Zonal wind velocity (left) and meridional wind velocity (right) simulated by the ECMWF T319 model at 10°E, 58°N on 2 March 2000, at 0000 UT (solid), 0600 UT (dashed), and 1200 UT (dotted-dashed).

[37] These results support the fact that the observed wave packet was generated by the Norwegian mountains. The wave freely propagated to the stratosphere, since it encountered no critical or reflection levels during its propagation. This is emphasized on Figure 12, which shows the wind-velocity profiles at 10°E, 58°N.

[38] The zonal wind (u) is eastward throughout the troposphere and stratosphere, so the ground-based horizontal phase speed of the wave (close to zero for mountain waves) never matches the zonal velocity and thus no critical level occurs.

4. Overall Activity

[39] In the previous section, we have analyzed a strong gravity wave event that induced large mesoscale temperature fluctuations. In this section, we are interested in the global activity of gravity waves in the Arctic polar vortex as seen during the whole MIR flight. In particular, we wish to assess how frequently strong events (like the one reported in the previous section) occur. To do this, we analyze the flight segments where the balloon stays at an approximately constant altitude. Those sections correspond to day and night ceilings. The ceilings where the balloon exhibits large vertical excursions were excluded from the analysis. The analyzed segments are shown in Figure 13.

[40] Generally speaking, the ceilings last ~10 h and for each ceiling, a polynomial fit of the data was performed in order to remove the large-scale component of the observations. This component may be partly produced by the balloon behavior under changing radiative conditions and not only by large-scale geophysical motions. We then compute the variances associated with the remaining fluctuations. Note that, due to this processing, we put the emphasis on fluctuations induced by short-period gravity waves (i.e., gravity waves with intrinsic periods less than 3 hours). *Dörnbrack et al.* [2002] have shown that longer-period inertia-gravity waves may also lead to significant temperature fluctuations above mountains. Yet, temperature fluctuations must vanish for waves whose intrinsic frequency tends to the inertial frequency [e.g., *Andrews et al.*, 1987].

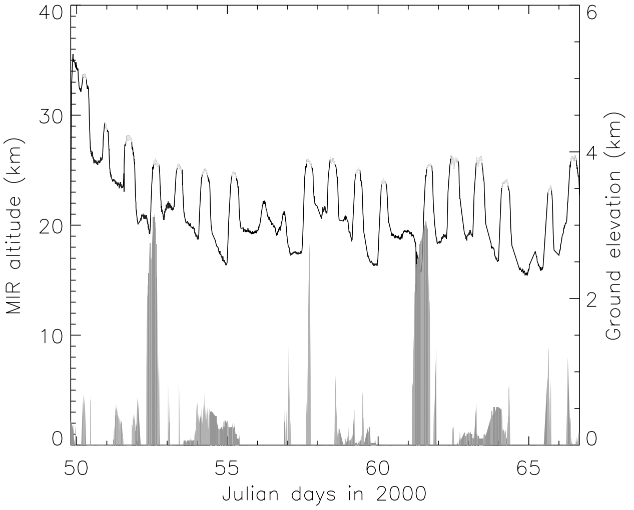

Figure 13. Altitude of the MIR during the flight (left scale). Day and night ceilings that have been analyzed for gravity wave activity are shown in red and blue, respectively. The ground elevation below the MIR is also shown (filled, right scale). See color version of this figure at back of this issue.

[41] We compute the mean amplitude ($\hat{X}'$) of the disturbances induced by gravity wave perturbations ($X'(t)$) during the flight as:

$$\hat{X}' = \frac{1}{J}\sum_i \sqrt{2\left(\overline{X'^2(t)}\right)_i}, \qquad (8)$$

where J is the number of ceilings, i is the *ith* ceiling, and $X'(t)$ is replaced respectively by the fluctuations of zonal and meridional wind velocities and air temperature (i.e., u', v' and T') measured on board the balloon. The analysis is performed for day and night ceilings separately (however, the amplitude of daytime temperature fluctuations is not shown, since temperature records are not useful during daylight). The results are reported in Table 2.

[42] The mean amplitudes are much smaller than the amplitude reported for the case study near southern Norway. This underlines the fact that waves similar to the one presented in the previous section are quite rarely observed on a global basis. Indeed, strong gravity wave events were only observed above mountains when the generation and propagation conditions were favorable, as in Figure 12. For instance, we also observed mountain waves when the balloon flew over Spitzbergen on day 53 at night (i.e., with accurate temperature measurements) and over the Urals on day 63. MWFM simulated temperature amplitudes were found to be in close agreement with the observations for these cases, i.e., ~3 K and 5 K respectively. However, we

Table 2. Mean Amplitude of Fluctuations Induced by Gravity Waves Along the Flight

Ceiling	$\hat{u}'$	$\hat{v}'$	$\hat{T}'$
Night (~21 km)	2.4 m s^{-1}	2.3 m s^{-1}	1 K
Day (~26 km)	3.4 m s^{-1}	3.4 m s^{-1}	–

Table 3. Mean Maximum Fluctuations Induced by Gravity Waves Along the Flight

Ceiling	$\hat{u}'$	$\hat{v}'$	$\hat{T}'$
Night (~21 km)	3.9 m s^{-1}	4.0 m s^{-1}	2.2 K
Day (~26 km)	5.9 m s^{-1}	5.2 m s^{-1}	–

did not observe waves during the two other balloon passes over Scandinavia nor above flat terrain. Furthermore, very similar gravity wave amplitudes (i.e., 2.5 m s^{-1}, 2.6 m s^{-1} and 1 K for zonal velocity, meridional velocity, and temperature fluctuations respectively) were observed during the 1999 flights (see, e.g., *Knudsen et al.* [2002] for the description of those flights) and confirms the values reported in Table 2 for background gravity wave activity. [*Pommereau et al.*, 1999] also reported a mean amplitude of temperature fluctuations close to 1 K associated with mesoscale events during the flights of two MIRs in the 1997 northern polar vortex.

[43] It should be stressed, however, that *Dörnbrack and Leutbecher* [2001] found that favorable conditions for the generation and propagation of gravity waves in Scandinavia preferentially occur in early winter (January and December) rather than in February, April and March. Therefore our results may reflect this intraseasonal variation of gravity wave activity and may be somewhat biased toward low values, since the MIR flights always occurred after mid-February.

[44] Another quantity that can be computed is the mean maximum fluctuation induced by gravity waves per ceiling, i.e.,:

$$\tilde{X}' = \frac{1}{J}\sum_i \max(X_i'), \tag{9}$$

with the same notation as before. The corresponding results are reported on Table 3. The maximum fluctuations are significantly higher than the mean amplitude fluctuations. This emphasizes the fact that the amplitude of the wave fluctuations measured by the MIR do not remain constant throughout a given day or night ceiling. Indeed, orographic waves generally induce a few oscillations located just in the mountain lee (see, e.g., the case study in this article or *Dörnbrack et al.* [2002]). However, the mean maximum amplitudes are still lower than those reported for the case study, which confirms that large-amplitude events are statistically rare.

5. Conclusions

[45] This study reported on in situ observations that were obtained by long-duration balloons able to drift for several weeks in the polar vortex. Such balloons allow us to acquire a global view of mesoscale processes in the lower stratosphere, within a quasi-Lagrangian frame of reference. We analyzed gravity wave activity in the Arctic stratospheric vortex during the 1999/2000 winter as it was observed during one of these balloon flights.

[46] In particular, we studied a strong gravity wave event that was observed above Scandinavia on 2 March 2000. It was shown that flow across mountains was the most likely generation mechanism of the observed wave packet. The amplitude of temperature disturbances is found to be 18 K peak to peak. Thus such large-amplitude gravity waves significantly alter the large-scale temperature field in the lower stratosphere and may enhance PSC formation.

[47] The observations were compared with various numerical simulations. Mesoscale models and ray-tracing simulations performed with respectively MM5 and MWFM succeeded in capturing the salient features of the observed gravity wave packet. Most of the simulated gravity wave characteristics agree reasonably with the observations, even though some were found to be less well reproduced. The ECMWF GCM also qualitatively captured the generation of the wave packet by the Scandinavian mountains. However, the simulated period and horizontal wavelength were overestimated by the ECMWF model, while the simulated amplitudes were significantly underestimated. This was interpreted to be a consequence of the divergence filtering in the ECMWF model. Thus the misrepresentation of gravity waves in GCMs can be responsible for part of the reported discrepancies between the observed temperatures in the stratosphere and those that are simulated by GCMs [*Knudsen et al.*, 2001].

[48] The overall gravity wave activity during the MIR flight was found to be much lower than in the case study. For instance, background amplitude of temperature fluctuations are found to be ~1 K (2 K peak to peak), similar to background values used in microphysical simulations [*Bacmeister et al.*, 1999]. Those experimental results support the fact that strong gravity wave events are mainly localized above mountains in the Arctic lower stratosphere and are quite rarely observed from a global point of view (at least during late winter and spring). Indeed, favorable generation conditions (strong low-level wind almost perpendicular to mountain ridges) and propagation conditions up to the stratosphere must be simultaneously met for large-amplitude waves to develop in the lower stratosphere. The occurrence of such conditions can induce an intraseasonal cycle of the gravity wave activity in the polar vortex, with strong activity in early winter and low activity in late winter and spring [e.g., *Dörnbrack and Leutbecher*, 2001]. Further observational studies are needed to assess this cycle more precisely.

[49] **Acknowledgments.** The authors would like to thank the various CNES teams at Kiruna for the successful MIR flights, and especially M. Durand for the Samba measurements. This work was done while AH was supported by EC grant ENV4-C T97-0504. SDE acknowledges support for this work through the Office of Naval Research and NASA's Atmospheric chemistry Modeling and Analysis Program (grant number W-19946). The Lagrangian project was supported by Programme National de Chimie de l'Atmosphère (PNCA), CNES, and the Research DG of the European Commission (EC contract ENV4-C T97-0504).

References

Allen, S. J., and R. A. Vincent, Gravity wave activity in the lower atmosphere: Seasonal and latitudinal variations, *J. Geophys. Res.*, *100*, 1327–1350, 1995.

Andrews, D. G., J. R. Holton, and C. B. Leovy, *Middle Atmosphere Dynamics*, San Diego, Calif., 1987.

Bacmeister, J. T., P. A. Newman, B. L. Gary, and K. R. Chan, An algorithm for forecasting mountain wave related turbulence in the stratosphere, *Weather Forecasting*, *9*, 241–253, 1994.

Bacmeister, J. T., S. D. Eckermann, P. A. Newman, L. Lait, K. R. Chan, M. Loewenstein, M. H. Proffitt, and B. L. Gary, Stratospheric horizontal wave number spectra of winds, potential temperature, and atmospheric tracers observed by high-altitude aircraft, *J. Geophys. Res.*, *101*, 9441–9470, 1996.

Bacmeister, J. T., S. D. Eckermann, A. Tsias, K. S. Carslaw, and T. Peter, Mesoscale temperature fluctuations induced by a spectrum of gravity waves: A comparison of parameterizations and their impact on stratospheric microphysics, *J. Atmos.*, *56*, 1913–1924, 1999.

Broutman, D., J. W. Rottman, and S. D. Eckermann, A hybrid method for analyzing wave propagation from a localized source, with application to mountain waves, *Q. J. R. Meteorol. Soc.*, *127*, 129–146, 2001.

Carslaw, K. S., et al., Increased stratospheric ozone depletion due to mountain-induced atmospheric waves, *Nature*, *391*, 675–678, 1998a.

Carslaw, K. S., et al., Particle microphysics and chemistry in remotely observed mountain polar stratospheric clouds, *J. Geophys. Res.*, *103*, 5785–5796, 1998b.

Carslaw, K. S., T. Peter, J. T. Bacmeister, and S. D. Eckermann, Widespread solid particle formation by mountain waves in the Arctic stratosphere, *J. Geophys. Res.*, *104*, 1827–1836, 1999.

Cot, C., and J. Barat, wave turbulence interaction in the stratosphere: A case study, *J. Geophys. Res.*, *91*, 2749–2756, 1986.

Coy, L., and R. Swinbank, Characteristics of stratospheric winds and temperatures produced by data assimilation, *J. Geophys. Res.*, *102*, 25,763–25,781, 1997.

Dean-Day, J., K. R. Chan, S. W. Bowen, T. P. Bui, B. L. Gary, and M. J. Mahoney, Dynamics of Rocky Mountain lee waves observed during SUCCESS, *Geophys. Res. Lett.*, *25*, 1351–1354, 1998.

Dörnbrack, A., and M. Leutbecher, Relevance of mountain wave cooling for the formation of polar stratospheric clouds over Scandinavia: A 20 year climatology, *J. Geophys. Res.*, *106*, 1583–1593, 2001.

Dörnbrack, A., M. Leutbecher, J. Reichardt, A. Behrendt, K. P. Müller, and G. Baumgarten, Relevance of mountain wave cooling for the formation of polar stratospheric clouds over Scandinavia: Mesoscale dynamics and observations for January 1997, *J. Geophys. Res.*, *106*, 1569–1581, 2001.

Dörnbrack, A., T. Birner, A. Fix, H. Flentje, A. Meister, H. Schmid, E. V. Browell, and M. J. Mahoney, Evidence for inertia gravity waves forming polar stratospheric clouds over Scandinavia, *J. Geophys.*, *107*, doi:10.1029/2001JD000452, in press, 2002.

Dudhia, J., A non-hydrostatic version of the Penn State-NCAR mesoscale model: Validation tests and simulation of an Atlantic cyclone and cold front, *Mon. Weather Rev.*, *121*, 1493–1513, 1993.

Eckermann, S. D., Hodographic analysis of gravity waves: Relationships among Stokes parameters, rotary spectra, and cross-spectral methods, *J. Geophys.*, *101*, 19,169–19,174, 1996.

Eckermann, S. D., and W. K. Hocking, Effect of superposition on measurements of atmospheric gravity waves: A cautionary note on some reinterpretations, *J. Geophys. Res.*, *94*, 6333–6339, 1989.

Eckermann, S. D., and P. Preusse, Global measurements of stratospheric mountain waves from space, *Science*, *286*, 1534–1537, 1999.

Fritts, D. C., and T. E. VanZandt, Effects of Doppler shifting on the frequency spectra of atmospheric gravity waves, *J. Geophys. Res.*, *92*, 9723–9732, 1987.

Gary, B. L., Observational results using the microwave temperature profiler during the airborne Antarctic ozone experiment, *J. Geophys. Res.*, *94*, 11,223–11,231, 1989.

Grell, G. A., J. Dudhia and D. R. Stauffer, A description of the fifth-generation Penn State/NCAR mesoscale model (MM5), *Tech. Note 398*, Nat. Cent. for Atmos. Res., Boulder, Colo., 1994.

Hertzog, A., and F. Vial, A study of the dynamics of the equatorial lower stratosphere by use of ultra-long-duration balloons, 2 Gravity waves, *J. Geophys. Res.*, *106*, 22,745–22,761, 2001.

Hines, C. O., Tropopausal mountain waves over Arecibo: A case study, *J. Atmos. Sci.*, *46*, 476–488, 1989.

Hirota, I., and T. Niki, A statistical study of inertia-gravity waves in the middle atmosphere, *J. Meteorol. Soc. Jpn.*, *63*, 1055–1066, 1985.

Knudsen, B. M., J.-P. Pommereau, A. Garnier, M. Nunez-Pinharanda, L. Denis, G. Letrenne, M. Durand, and J. M. Rosen, Comparison of stratospheric air parcel trajectories based on different meteorological analyses, *J. Geophys. Res.*, *106*, 3415–3424, 2001.

Knudsen, B. M., J. P. Pommereau, A. Garnier, M. Nunez-Pinharanda, L. Denis, P. Newmann, G. Letrenne, and M. Durand, Accuracy of analyzed stratospheric temperatures in the winter Arctic vortex from infrared Montgolfier long-duration balloon flights, 2, Results, *J. Geophys.*, *107*, doi:10.1029/2001JD001329, in press, 2002.

Leutbecher, M., and H. Volkert, The propagation of mountain waves into the stratosphere: quatitative evaluation of three-dimensional simulations, *J. Atmos. Sci.*, *57*, 3090–3108, 2000.

Lott, F., and M. J. Miller, A new subgrid-scale orographic drag parametrization: Its formulation and testing, *Q. J. R. Meteorol. Soc.*, *123*, 101–127, 1997.

Marks, C. J., and S. D. Eckermann, A three-dimensional nonhydrostatic ray-tracing model for gravity waves: Formulation and preliminary results for the middle atmosphere, *J. Atmos.*, *52*, 1959–1984, 1995.

Massman, W. J., On the nature of vertical oscillations of constant volume balloons, *J. Appl. Meteorol.*, *17*, 1351–1356, 1978.

Massman, W. J., An investigation of gravity waves on a global scale using TWERLE data, *J. Geophys. Res.*, *86*, 4072–4082, 1981.

Moldovan, H., F. Lott, and H. Teitelbaum, Wave breaking and critical levels for propagating inertio-gravity waves in the lower stratosphere, *Q. J. R. Meteorol. Soc.*, *128*, 713–732, 2002.

Murphy, D. M., and B. L. Gary, Mesoscale temperature fluctuations and polar stratospheric clouds, *J. Atmos. Sci.*, *52*, 1753–1760, 1995.

O'Sullivan, D., and T. J. Dunkerton, Generation of inertia-gravity waves in a simulated life cycle of baroclinic instability, *J. Atmos. Sci.*, *52*, 3695–3716, 1995.

Pawson, S., B. Naujokat, and K. Labitzke, On the polar stratospheric cloud formation potential of the northern stratosphere, *J. Geophys. Res.*, *100*, 23,215–23,225, 1995.

Peter, T., Microphysics and heterogeneous chemistry of polar stratospheric clouds, *Annu. Rev. Phys. Chem.*, *48*, 785–822, 1997.

Pommereau, J.-P., P. Cseresnjes, L. Denis, and A. Hauchecorne, Stratospheric temperature measurements in the winter Arctic vortex in 1997 onboard long duration balloons: Comparison to ECMWF model and detection of orographic waves, in *Mesoscale Processes in the Stratosphere*, *Air Pollut. Res. Rep. 69*, edited by K. S. Carslaw and G. Amanatidis, pp. 11–216, Cordis RTD Publ., Luxembourg, 1999.

Pommereau, J.-P., et al., Accuracy of analyzed stratospheric temperatures in the winter Arctic vortex from infrared Montgolfier long-duration ballon flights, 1, Measurements, *J. Geophys. Res.*, *107*, 8260, doi:10.1029/2001JD001379, 2002.

Rabier, F., H. Järvinen, E. Klinker, J.-F. Mahfouf, and A. Simmons, The ECMWF operational implementation of four dimensional variational assimilation, I, Experimental results with simplified physics, *Q. J. R. Meteorol. Soc.*, *126*, 1143–1170, 2000.

Rivière, E. D., et al., Role of lee waves in the formation of solid polar stratospheric clouds: Case studies from February 1997, *J. Geophys. Res.*, *105*, 6845–6853, 1997.

Schoeberl, M. R., The penetration of mountain waves into the middle atmosphere, *J. Atmos. Sci.*, *42*, 2856–2864, 1985.

Solomon, S., Stratospheric ozone depletion: A review of concepts and history, *Rev. Geophys.*, *37*, 275–316, 1999.

Vial, F., A. Hertzog, C. R. Mechoso, C. Basdevant, P. Cocquerez, V. Dubourg, and F. Nouel, A study of the dynamics of the equatorial lower stratosphere by use of ultra-long-duration balloons, 1, Planetary scales, *J. Geophys. Res.*, *106*, 22,725–22,743, 2001.

Vincent, R. A., and S. D. Eckermann, VHF radar observations of mesoscale motions in the troposphere: Evidence for gravity wave Doppler shifting, *Radio Sci.*, *25*, 1019–1037, 1990.

Wirth, M., and W. Renger, Evidence of large scale ozone depletion within the Arctic polar vortex 94/95 based on airborne LIDAR measurements, *Geophys. Res. Lett.*, *23*, 813–816, 1996.

A. Dörnbrack, Institut für Physik der Atmosphäre, DLR Oberpfaffenhofen, D-82230 Wessling, Germany. (Andreas.Doernbrack@dlr.de)

S. D. Eckermann, Naval Research Laboratory, 4555 Overlook Ave., S.W., Washington, DC 20375, USA. (eckermann@uap2.nrl.navy.mil)

A. Hertzog and F. Vial, Laboratoire de Météorologie Dynamique, École Polytechnique, F-91128 Palaiseau Cedex, France. (albert.hertzog@lmd.polytechnique.fr; francois.vial@lmd.polytechnique.fr)

B. M. Knudsen, Danish Meteorological Institute, Lyngbyvej 100, 2100 Copenhagen, Denmark. (bk@dmi.dk)

J.-P. Pommereau, Service d'Aéronomie, BP3, F-91371 Verrières-le-Buisson Cedex, France. (pommereau@aerov.jussieu.fr)

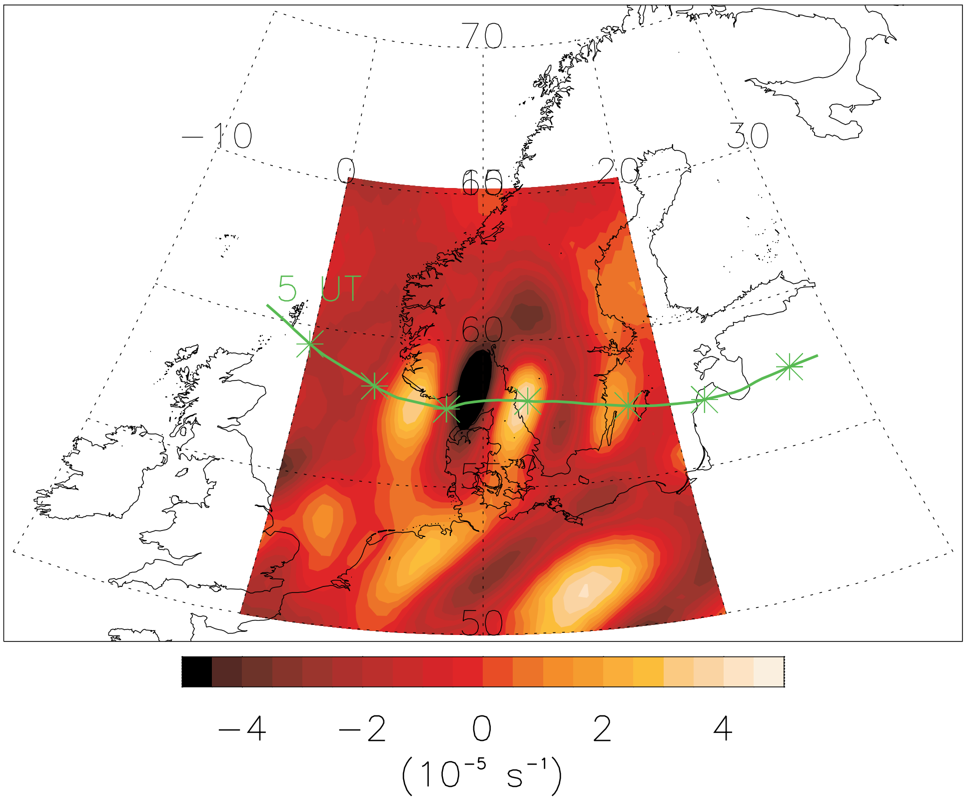

Figure 7. Divergence of the horizontal wind velocity simulated by the ECMWF T319 model at 20 hPa on 2 March 2000, 1200 UT. The trajectory of the balloon is shown in green and stars are plotted every 2 h.

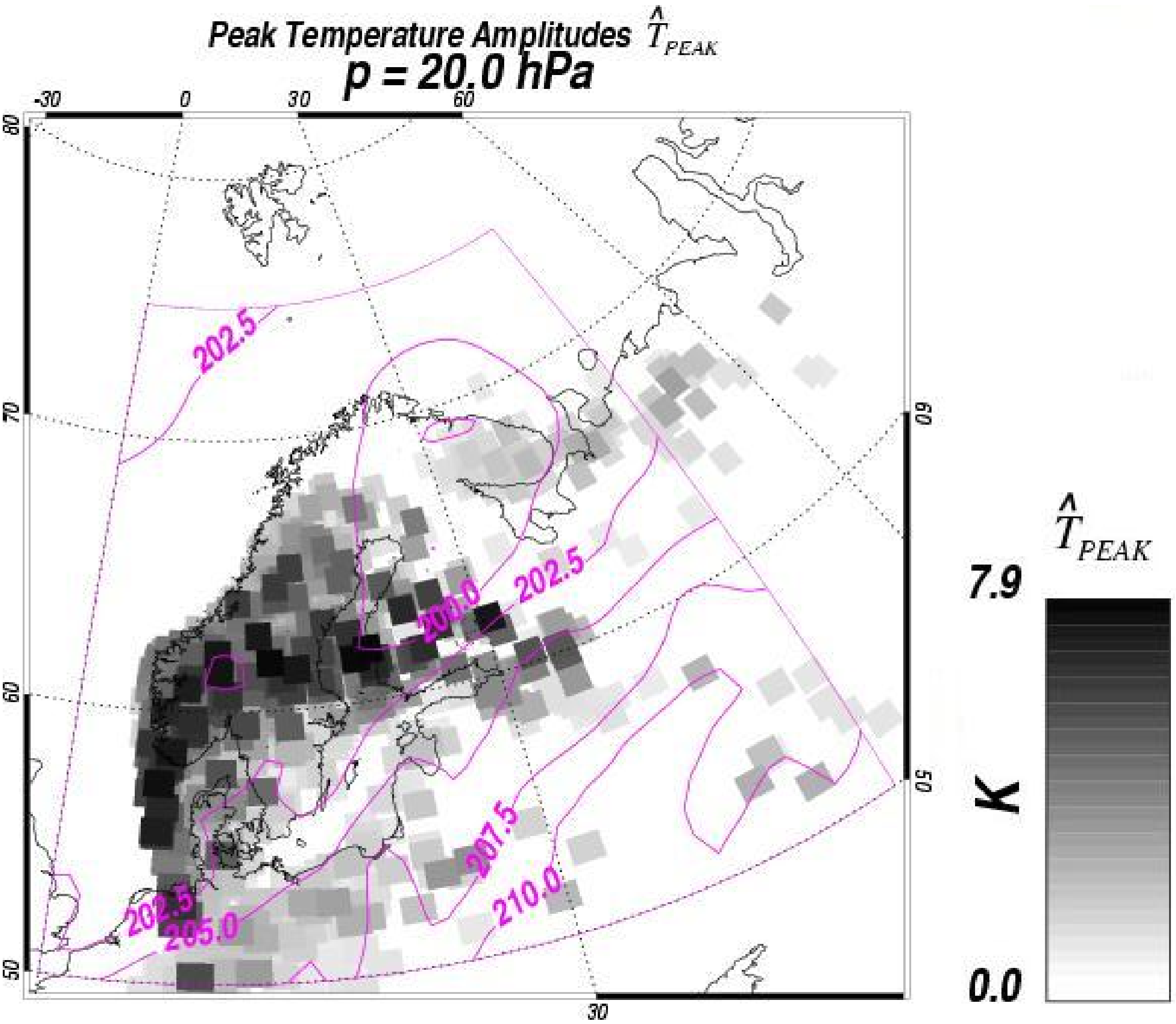

Figure 8. MWFM simulation of peak temperature amplitudes at 20 hPa on 2 March 2000, 0000 UT (colored squares). Each pixel represents the group location and amplitude of a ray. DAO analyzed background temperatures are represented as contours (labels in K).

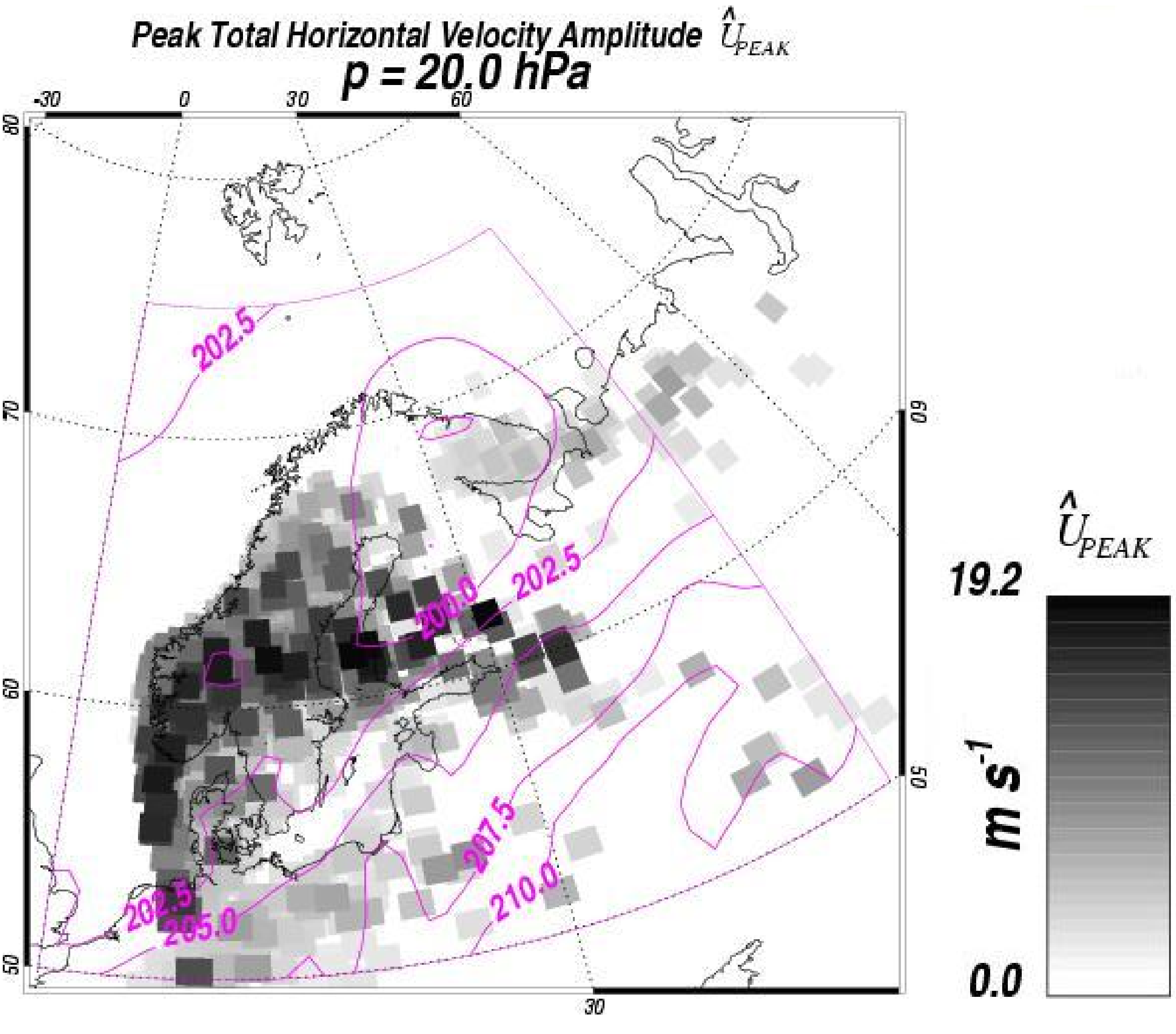

Figure 9. Same as Figure 8 but for the horizontal velocity.

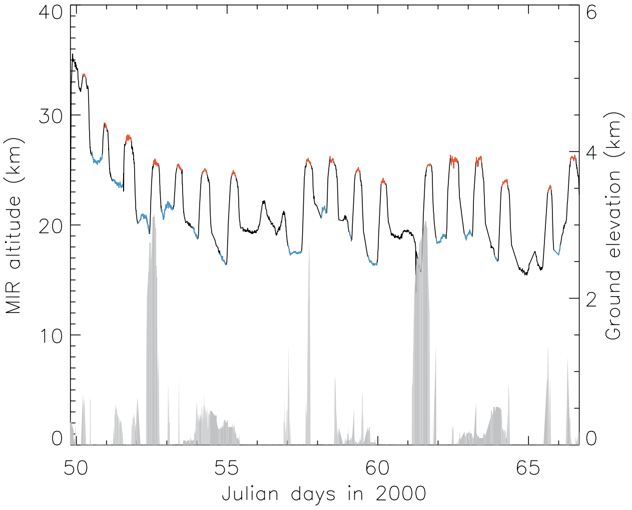

Figure 13. Altitude of the MIR during the flight (left scale). Day and night ceilings that have been analyzed for gravity wave activity are shown in red and blue, respectively. The ground elevation below the MIR is also shown (filled, right scale).